A&A, 687, A32 (2024)
https://doi.org/10.1051/0004-6361/202348941

Astronomy & Astrophysics

Quasars as standard candles

V. Accounting for the dispersion in the L_X–L_{UV} relation down to ≤ 0.06 dex

Matilde Signorini[1,2,3], Guido Risaliti[1,2], Elisabeta Lusso[1,2], Emanuele Nardini[2], Giada Bargiacchi[4,5], Andrea Sacchi[6], and Bartolomeo Trefoloni[1,2]

[1] Dipartimento di Fisica e Astronomia, Università di Firenze, Via G. Sansone 1, 50019 Sesto Fiorentino, Firenze, Italy
e-mail: matilde.signorini@unifi.it
[2] INAF – Osservatorio Astrofisico di Arcetri, Largo Enrico Fermi 5, 50125 Firenze, Italy
[3] University of California-Los Angeles, Department of Physics and Astronomy, PAB, 430 Portola Plaza, Box 951547, Los Angeles, CA 90095-1547, USA
[4] Scuola Superiore Meridionale, Largo S. Marcellino 10, 80138 Napoli, Italy
[5] Istituto Nazionale di Fisica Nucleare (INFN), Sez. di Napoli, Complesso Univ. Monte S. Angelo, Via Cinthia 9, 80126 Napoli, Italy
[6] Center for Astrophysics | Harvard & Smithsonian, 60 Garden Street, Cambridge, MA 02138, USA

Received 13 December 2023 / Accepted 22 March 2024

ABSTRACT

A characteristic feature of quasars is the observed non-linear relationship between their monochromatic luminosities at rest-frame 2500 Å and 2 keV. This relationship is evident across all redshifts and luminosities and, due to its non-linearity, can be implemented to estimate quasar distances and construct a Hubble Diagram for quasars. Historically, a significant challenge in the cosmological application of this relation has been its high observed dispersion. Recent studies have demonstrated that this dispersion can be reduced by excluding biased objects from the sample. Nevertheless, the dispersion remains considerable ($\delta \sim 0.20$ dex), especially when compared to the Phillips relation for supernovae Ia. Given the absence of a comprehensive physical model for the relation, it remains unclear how much of the remaining dispersion is tied to the physical mechanism behind the relation itself and how much can be attributed to other factors, not addressed by the sample selection and by the choice of X-ray and UV indicators. Potential contributing factors include (i) the scatter produced by using X-ray photometric results instead of spectroscopic ones, (ii) the intrinsic variability of quasars, and (iii) the inclination of the accretion disc relative to our line of sight. In this study, we thoroughly examine these three factors and quantify their individual contributions to the observed dispersion. Based on our findings, we argue that the characteristic dispersion of the X-ray–UV luminosity relationship (which is attributable to the physical mechanism behind it) is likely below 0.06 dex. This result reinforces the validity of using quasars as standard candles and offers valuable insights for developing physical models of the X-ray/UV relation. Achieving such a low dispersion on large observed data sets is hardly feasible, due to the complexity of removing all the empirical contributions to the scatter. Nevertheless, we argue that high-redshift subsamples can show a significantly lower dispersion than the average subsample. This aspect is particularly significant for cosmological applications, indicating that targeted observations of select high-redshift objects can enhance the cosmological power of quasars in constraining the shape of the Hubble Diagram at high redshift.

Key words. methods: statistical – galaxies: active – quasars: general – quasars: supermassive black holes

1. Introduction

Quasars, the most luminous and persistent sources in the Universe, are now observed up to redshift $z \simeq 7.5$ (Mortlock et al. 2011; Bañados et al. 2018; Wang et al. 2021). Their spectral energy distribution (SED) spans from the radio to the X-ray band, with the most intense emission observed at optical–UV wavelengths (e.g. Sanders et al. 1989; Richards et al. 2006; Elvis et al. 2012). The bulk of this emission is interpreted to originate in an optically thick accretion disc surrounding the central supermassive black hole (SMBH; Shakura & Sunyaev 1973).

A consistent feature of quasars is the presence of the non-linear relation between their X-ray and UV luminosities, often represented as $\log(L_X) = \gamma \log(L_{UV}) + \beta$, with a slope $\gamma \simeq 0.6$ (e.g. Steffen et al. 2006; Lusso et al. 2010; Young et al. 2010). This relation has been known for decades (e.g. Tananbaum et al. 1979), and it has been observed to hold over a wide range of redshifts and luminosities. Its presence suggests a strong interaction between the UV-emitting accretion disc and the X-ray corona, but the exact mechanism behind it remains elusive.

The L_X–L_{UV} relation has far-reaching implications, not only for quasar physics, but also for cosmology. The non-linearity and consistency of the relation allow us to determine cosmological distances and therefore use quasars as standard candles. Such a possibility has been acknowledged since the discovery of the relation, but it had not been successfully implemented due to the high observed dispersion (∼0.40 dex), which made any application for cosmological purposes challenging.

Recent studies have shown that most of this 0.40 dex dispersion arises from observational effects that can for the most part be removed by filtering out biased objects (Risaliti & Lusso 2015; Lusso & Risaliti 2016; Lusso et al. 2020). By removing quasars affected by dust reddening, gas absorption, or that might suffer from Eddington bias, the dispersion reduces significantly, down to $\delta \sim 0.20$ dex, making quasars an actually useful cosmological tool. The development in terms of the dispersion reduction has enabled the extension of the Hubble Diagram to higher redshift values than those achievable with supernovae Ia (SN Ia). The extended Hubble diagram of quasars and

supernovae abides by the predictions of a flat ΛCDM cosmology up to redshift $z \sim 1.5$, but a 4σ tension shows up at higher redshifts (Risaliti & Lusso 2019; Lusso et al. 2020). This tension has been confirmed when investigated in a cosmology-independent way (e.g. Bargiacchi et al. 2021, 2022; Giambagli et al. 2023), and it has recently been retrieved also with a UV spectroscopically validated sample of ∼1800 objects (Signorini et al. 2023a).

At the same time, the remaining, rather high, dispersion of the relation between luminosities is still one of the biggest issues for both the implementation of quasars as standard candles and our understanding of the physical process behind it.

This observed dispersion has two components: the first is accounted for by the uncertainties on the luminosity estimates, while the latter is an intrinsic dispersion δ that we need to introduce because the uncertainties alone are not enough to explain the observed scatter of the points around the best-fit relation. This δ parameter is usually a free parameter in our fits of the L_X−L_{UV} relation (Risaliti & Lusso 2019; Lusso et al. 2020; Signorini et al. 2023a), which we include with no preconception about its origin or physical meaning. In this framework, it simply represents the amount of scatter we need to consider to explain the total observed scatter, on top of the uncertainties on luminosities. In other words, the total scatter of the points around the best-fit relation is given by the quadratic sum of the uncertainties on the luminosity measurements with the intrinsic dispersion parameter δ.

In principle, this intrinsic dispersion has different components. One is the "characteristic" dispersion of the relation, that is, the dispersion due to the physical mechanism behind the relation. This characteristic dispersion cannot be removed, although its value might be different for objects with different physical properties. As we still lack a universally accepted physical explanation for the L_X−L_{UV} relation, we cannot currently give a theoretical estimate of this quantity. There are then additional factors that are not tied to the physics of the relation, but at the same time cannot be removed with the sample selection. These factors can be physical or geometrical, like quasar variability and orientation with respect to the line of sight, or observational, like the choice of different UV and X-ray proxies, or the use of spectroscopic over photometric estimates of UV and X-ray fluxes. How much of the ∼0.20 dex dispersion is due to the characteristic dispersion of the relation δ_{char}, rather than to the residual additional factors δ_{res} (either physical or observational), and how much of these contributions can be reduced or removed, are still open questions.

Recent studies have started to address these questions. For example, Sacchi et al. (2022) reported a reduced intrinsic dispersion of 0.09 dex for a subset of 30 quasars at redshift $3.0 < z < 3.3$. This subset, despite its specific selection criteria[1] shows UV and X-ray properties consistent with the broader quasar population. Furthermore, Signorini et al. (2023a) have demonstrated that, with the right selection of UV and X-ray proxies, it is possible to reduce the intrinsic dispersion for a much larger sample from ∼0.20 dex down to ∼0.16 dex.

These findings suggest that the characteristic dispersion of the L_X−L_{UV} relation is low and that much of the intrinsic dispersion is linked to residual factors (physical and observational). In this paper our aim is to investigate in detail these factors. We seek to quantify their contribution to the total observed dispersion and estimate the true characteristic dispersion of the L_X−L_{UV} relation.

[1] This interval contains 15 sources for which high-quality *XMM-Newton* pointed observations were obtained (Nardini et al. 2019; Sacchi et al. 2022).

In this work, we address three main contributors to the residual dispersion: X-ray variability, the inclination of the accretion disc relative to our line of sight, and potential biases in X-ray flux estimates via photometry. We consider the total dispersion, δ, as a combination of the characteristic dispersion of the L_X−L_{UV} relation, δ_{char}, and the dispersion introduced by additional issues, δ_{res}. With no universally accepted model explaining the L_X−L_{UV} relation yet, our approach focuses on determining δ_{res} to better constrain and understand δ_{char}. Through this approach, we aim to provide valuable insights into this relationship and support the implementation of quasars in cosmology.

The paper is structured as follows: in Sect. 2 we describe the parent sample and the observational biases that have already been removed with its selection; in Sect. 3 we investigate the contribution of the variability to the observed dispersion. In Sect. 4 we consider the contribution of inclination, providing an estimate through the use of a mock sample of quasars, while in Sect. 5 we focus on the possible contribution of using X-ray photometric data instead of spectroscopic ones. In Sect. 6 we compare our findings with the observational results about the dispersion, and in Sect. 8 we draw our conclusions.

2. Sample selection

For this work, we considered the objects selected in Lusso et al. (2020, hereafter L20). This sample is made up of ∼2400 quasars, all of which have available UV and X-ray data in public catalogues. As discussed in L20, these objects have been selected in order to remove biased sources, and this process allowed us to reduce the observed dispersion from ∼0.40 dex to ∼0.20 dex. Here we briefly discuss these removable sources of bias; more details are given in Sect. 5 of L20.

BAL and radio-loud quasars. The UV fluxes of broad absorption line (BAL) quasars can be heavily affected by gas (and dust) absorption and, as a consequence, these objects will deviate from the L_X−L_{UV} relation. Radio-loud quasars, instead, possibly show a jet-related X-ray component that adds to the one emitted by the corona, so they are supposed to deviate from the L_X−L_{UV} relation too. Quasars flagged as either BAL or radio-loud are therefore excluded from the sample.

Dust extinction. In principle, dust extinction could affect to some extent most of the observed quasars. Since dust reddening has a stronger impact on the UV band than on the X-rays, its contribution can significantly alter the L_X−L_{UV} relation. To minimise this effect, the sample was selected as described in Lusso & Risaliti (2016): for each quasar the slopes Γ_1 and Γ_2 of the $\log(\nu) - \log(\nu L_\nu)$ power-law continuum in the 0.3−1 μm and in the 1450−3000 Å range were computed. Then, it was considered the point in the Γ_1−Γ_2 plane that corresponds to the SED of Richards et al. (2006) with zero extinction, which is at $\Gamma_1 = 0.82$ and $\Gamma_2 = 0.40$. The objects whose values of Γ_1−Γ_2 fell into the circle centred in 0.82−0.40 ($E(B-V) = 0.0$), with a radius of 1.1 (which corresponds to $E(B-V) \simeq 0.1$) were selected, while those which fell outside this range were removed from the sample.

Eddington bias. If the intrinsic X-ray flux of a quasar is close to the flux limit of a given observation, it will be detected only if a fluctuation towards higher fluxes takes place, while it will not be detected otherwise. This effect clearly introduces a potential bias in our sample. To avoid it, only sources that would remain above the flux limit even in case of a negative flux fluctuation were selected.

X-ray absorption. In the X-ray band, photoelectric absorption can take place due to the presence of gas in the quasar's rest frame. This gas absorption modifies the X-ray spectral shape; particularly, the effect in spectra of moderate quality is to lower the observed photon index Γ of the X-ray continuum power law. The distribution of Γ usually peaks around 1.9–2.0 for unobscured, luminous quasars (e.g. Young et al. 2009), and Γ exceeds 1.7 for almost all the sources with high-quality spectra. Therefore, to minimise this effect, only quasars with $\Gamma > 1.7$ were selected. Furthermore, objects with $\Gamma > 2.8$ are excluded too, to avoid soft-excess contribution at $z \lesssim 1$ (e.g. Sobolewska & Done 2007; Gliozzi & Williams 2020).

3. Variability

Quasars exhibit non-periodic and stochastic variability across all observed wavelengths (Vanden Berk et al. 2004; Markowitz & Edelson 2004), occurring on timescales ranging from hours (Ponti et al. 2012) to years (de Vries et al. 2005; Vagnetti et al. 2011). Despite significant efforts, the underlying mechanisms driving this variability are still not completely understood. Notably, an observed anti-correlation between luminosity and variability has been established (Hook et al. 1994; Kelly et al. 2009; Lanzuisi et al. 2014; Paolillo et al. 2017), attributed to the influence of black-hole mass and accretion rate on the variability pattern (Prokhorenko et al. 2024).

The timescales of quasar variability are wavelength-dependent, with X-ray emission displaying considerably faster variability compared to the optical band. In the context of the L_X–L_{UV} relation this means that, because of the nature of variability, the same UV state corresponds to a range of X-ray states. Therefore, even if the characteristic dispersion of the L_X–L_{UV} relation were null, this would introduce a scatter in the observed relation. Given that X-ray variability exhibits the largest amplitude on comparable timescales, it contributes most significantly to the observed dispersion. In this section, we give an estimate of this contribution for the objects in the L20 sample.

To do so, we looked for the objects in the L20 sample that have more than one serendipitous observation in the *XMM-Newton* source catalogue 4XMM–DR9 (Webb et al. 2020). We found 289 objects with multiple observations; the vast majority (80%) has only two observations, so we considered the longest and the second longest observation for each object. Our goal was to compare the monochromatic 2 keV luminosities obtained from two observations that happened at random different times; we expected them to follow a one-to-one relation, with a scatter that would give us an estimate of the variability contribution to the dispersion in the L_X–L_{UV} relation. So we fit the relation between the second longest ($L_{X,2}$) and the longest ($L_{X,1}$) observations with a line: $\log(L_{X,2}) = \alpha \log(L_{X,1}) + \zeta$, with the slope α and the normalisation ζ as free parameters. We perform the comparison using logarithmic values of the luminosities because of the stochastic nature of variability, which is known to follow a log-normal flux distribution (e.g. Vaughan et al. 2003; Uttley et al. 2005). We have indeed tested that for the object with the largest number of observations (31), this is actually the case. The fit was performed with a Bayesian approach of likelihood maximisation; we used the `emcee` code, which is an implementation of Goodman and Weare's Affine Invariant Markov chain Monte Carlo (MCMC) Ensemble sampler (Foreman-Mackey et al. 2013). In building the likelihood, we need to consider that we have uncertainties of similar magnitude on both axes; to account for this, we adapted the BCES method (Akritas & Bershady 1996), where the tangent ellipse is used to measure the distance of each point form the best-fit line.

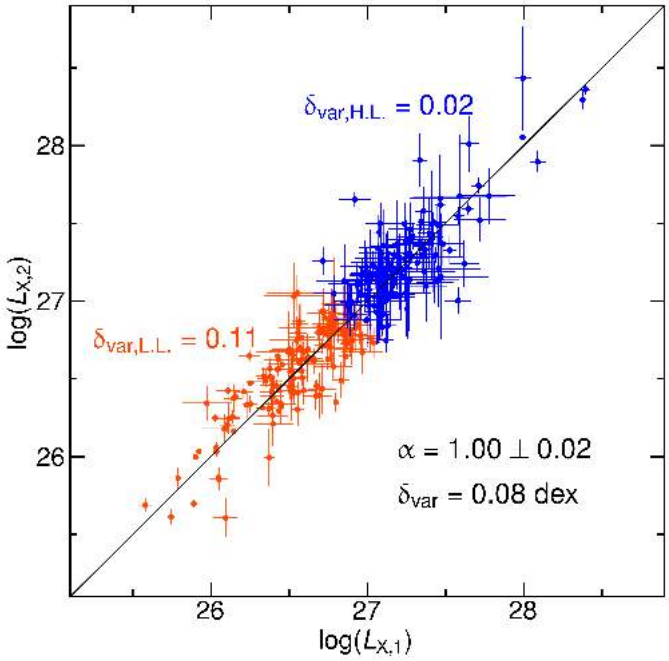

Fig. 1. Comparison of the 2-keV luminosities for objects with multiple X-ray observations. The best fit is consistent with the bisector line (solid line). The dispersion parameter due to variability is $\delta_{var} = 0.08$ dex. When distinguishing between the high- and low-luminosity subsamples, we see that δ_{var} is higher for lower luminosities. The difference between high and low luminosity is not visually discernible, as the total dispersion for the two subsample is nearly the same. However, while in the high-luminosity sample the observational uncertainties on the fluxes can almost completely explain the overall scatter, in the low-luminosity subsample a significant contribution associated to variability is required to explain the scatter we observe. Luminosities are derived from photometric fluxes, assuming a standard flat ΛCDM model. We note that, as we are comparing luminosities for the same object, the results do not depend on the chosen cosmological model.

The results are shown in Fig. 1. We obtained, as expected, a slope $\alpha = 1.00 \pm 0.02$, and an intercept value of $\zeta = -0.005 \pm 0.015$. We also derived the total dispersion of the relation as

$$\delta_{tot} = \sqrt{\sum_{i}^{N} \log(L_{X,2})_i^2 - (\alpha \log(L_{X,1})_i + \zeta)^2}, \quad (1)$$

which turns out to be 0.17 dex. If the uncertainties on the x- and y-axis completely explained this dispersion, no intrinsic scatter due to variability would be present. However, we computed the average observational uncertainty on both $\log(L_{X,1})$ and $\log(L_{X,2})$ and we obtained 0.15 dex. Given this result, we can compute the intrinsic dispersion due to variability simply as $\delta_{var} = \sqrt{\delta_{tot}^2 - \delta_{err}^2}$, and get $\delta_{var} = 0.08$ dex. This value can therefore be considered as the average contribution of X-ray variability to the dispersion in the L_X–L_{UV} relation. Although the number of objects for which we have multiple observations is only ∼12% of the total L20 sample, these objects are fully representative (given that the observations we are considering are serendipitous) and they span the same luminosity range as the whole sample. So we can consider the result from this analysis to be applicable to the whole quasar catalogue.

We note that a similar analysis on objects with multiple observations was performed in Lusso & Risaliti (2016), with a smaller sample of 159 objects, and they found the variability

contribution to be $\delta_{\rm var} = 0.12$ dex. Considering that the analysis described in this section was performed with a sample which is nearly doubled in statistics, and that the selection procedure has been improved from Lusso & Risaliti (2016), we believe our estimate of $\delta_{\rm var} = 0.08$ to be more accurate.

We also tested the dependence of variability on luminosity for our sample, by dividing it into two subsamples, above and below the value of $\log(L_{\rm X}) = 26.9$. The objects in the subsamples are 145 and 144, respectively, and for each of them we derived the total dispersion and the average uncertainty as described above. For the high-luminosity sample, we obtain a total dispersion of $\delta_{\rm tot,H.L.} = 0.185$ and an average uncertainty of $\delta_{\rm err,H.L.} = 0.184$. By quadratic subtraction we obtain that the amount of scatter due to variability is only $\delta_{\rm var,H.L.} = 0.02$ dex. Then, for the high-luminosity sample, the uncertainties on the flux estimates alone explain almost all the scatter we observe. For the low-luminosity sample, instead, we obtain a total dispersion of $\delta_{\rm tot,L.L.} = 0.171$ and an average uncertainty of $\delta_{\rm err,L.L.} = 0.131$. Therefore, the amount of scatter due to variability is $\delta_{\rm var,L.L.} = \sqrt{\delta^2_{\rm tot,L.L.} - \delta^2_{\rm err,L.L.}} = 0.11$ dex. Hence, for the low-luminosity sample, the observational uncertainties are not enough to explain the observed scatter around the best fit, and the contribution due to variability is not negligible.

These results are all shown in Fig. 1. We note that, visually, there is no detectable difference between the high- and the low-luminosity subsets. This is because the observed total dispersion is very similar for the two samples. However, in the former case the total dispersion is almost totally consistent with the one expected from the observational uncertainties. In the latter case, we need an additional contribution due to the variability to explain the observed total dispersion.

This difference between low- and high-luminosity objects is not only consistent with results in the literature, but it can, at least partially, also explain the results of Sacchi et al. (2022), where a dispersion as low as 0.09 dex is observed for a sample of objects at redshift $3.0 < z < 3.3$. Together with having spectroscopic data and mostly pointed X-ray observations, these objects have an average luminosity of $\log(L_{\rm X}/{\rm erg\,s^{-1}\,Hz^{-1}}) \sim 27.7$, which is in the high luminosity regime. Therefore, the contribution of variability to their total dispersion must be very little.

4. Inclination

The second factor contributing to the observed dispersion we are considering is the inclination of the quasar accretion disc relative to the line of sight. The optical–UV intrinsic emission from quasars is typically attributed to a disc-like component. The angle at which a quasar is viewed then crucially influences its observed flux. Specifically, unless the quasar is perfectly face-on, the observed flux, $f_{\rm obs}$, is derived from the intrinsic UV flux ($f_{\rm int}$) as $f_{\rm obs} = f_{\rm int}\cos\theta$, where θ is the angle between the observer's line of sight and the axis of the quasar's disc. Notably, while the inclination affects the observed UV flux, it has no effect on the X-ray flux. This distinction arises because X-ray coronal emission is believed to be isotropic. The exact location and geometry of the corona are still largely unknown, although polarisation results are now providing new perspectives on the topic (e.g. Gianolli et al. 2023). We note here that we assume the X-ray emission to be isotropic throughout this work.

This inclination effect, by changing the UV flux, changes the slope of the relation, differently for each different inclination angle. Overall this results in an increase in the observed dispersion for the global quasar sample. Moreover, this effect is asymmetric, impacting quasars differently based on their relative brightness with respect to the detection limit. Bright quasars, surpassing by far the detection threshold, will still be detected even with a diminished observed flux $f_{\rm obs}$ at large inclination angles. However, for quasars nearing the flux limit, there is a range of $\cos\theta$ values where they become undetectable.

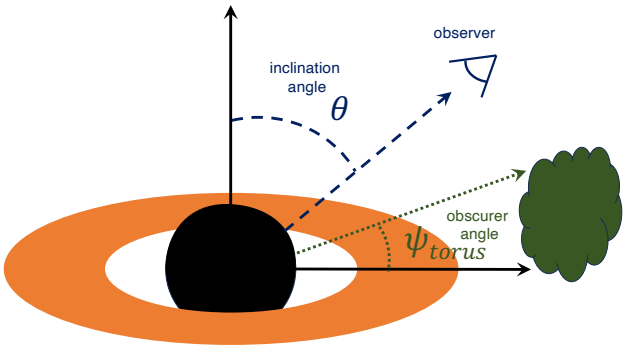

Fig. 2. Schematic representation of a quasar observed at a certain angle θ, measured from the axis of the accretion disc. If we assume the presence of an obscurer with a certain angular width $\psi_{\rm torus}$, measured from the disc surface, only the objects with an inclination angle between zero (face-on) and $\theta_{\rm max} = \pi/2 - \psi_{\rm torus}$ will be observed and/or selected.

In an ideal scenario, if we had accurate knowledge of the inclination angle θ for every quasar observed, we could correct the observed flux to counterbalance inclination effects. Unfortunately, we do not have consistent estimators for the inclination of quasars. Some works suggest that the intensity of the [O III] line is an indicator of the inclination angle of a quasar (e.g. Bisogni et al. 2017). Yet, this result is valid in a statistical sense, but cannot be reliably used for an object-by-object correction. Furthermore, this line escapes the SDSS spectral range for redshifts above ∼0.7.

Given that we lack observational methods to measure inclinations directly, we will tackle this challenge using mock samples of quasars. While we might not be able to eliminate this source of dispersion, we can estimate its contribution. This is essential for accurately determining the intrinsic dispersion of the $L_{\rm X}$–$L_{\rm UV}$ relation. In this section, we discuss how to build a mock sample of quasars to correctly represent the effect of inclination, and derive an estimate for its contribution to the total dispersion.

4.1. Correction to a luminosity function

The first step to build our mock sample is to determine from which luminosity distribution we should extract our objects. Numerous studies have established the observed UV luminosity function for quasars and its redshift evolution (e.g. Boyle et al. 2000; Croom et al. 2009; Ross et al. 2013). However, within a particular luminosity range, the quasars we observe are only those that, once inclined, have a flux above the survey flux limit. Consequently, the observed luminosity function for quasars is biased, and a priori we do not know how much the shape of the luminosity function changes because of that. Here we therefore attempt to deduce the intrinsic luminosity function of quasars from the observed one, and then use it as the starting point for our mock sample.

We designate θ as the inclination angle, signifying that a face-on quasar has $\theta = 0$ whilst an edge-on quasar has $\theta = \pi/2$, as shown in Fig. 2. We postulate that quasars are randomly inclined in the sky. For a given intrinsic luminosity $\mathcal{L}$, the

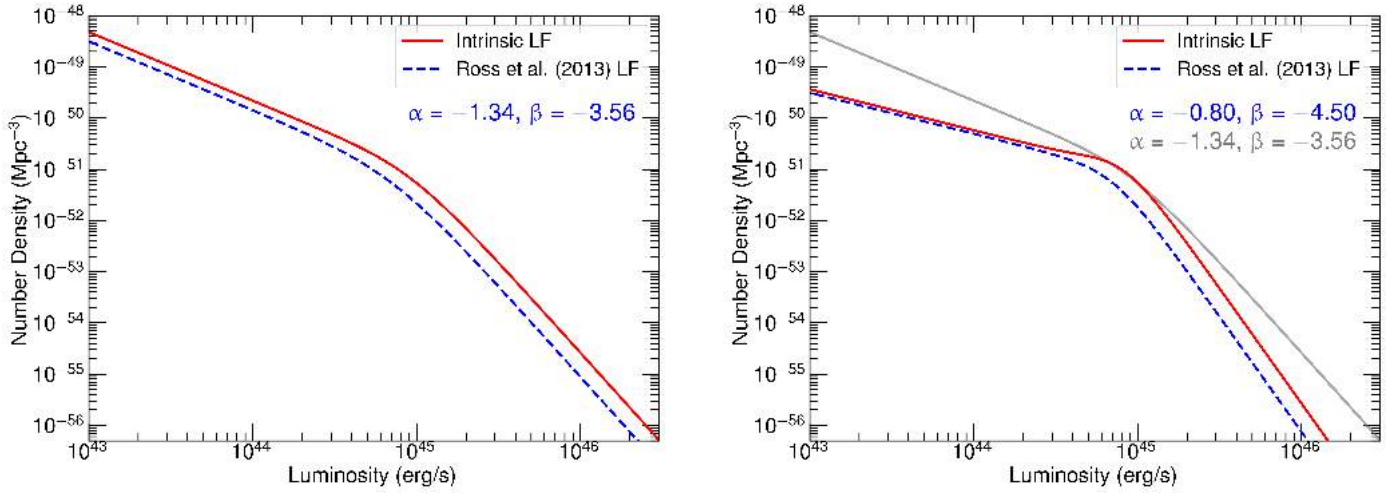

Fig. 3. Effect of inclination on the luminosity function shape, and how this effect depends on the slope values of the luminosity function. Left: observed luminosity function $n(L)$, in blue dashed, as per the Ross et al. (2013) parametrisation: the luminosity function is a broken power law with indexes $\alpha = -1.34$ and $\beta = -3.56$, and $\log(\phi_*) = -6.15$. A Pure Luminosity Evolution is assumed. In this figure we show, as an example, the results for $z = 1$. In solid red, the intrinsic luminosity function $m(\mathcal{L})$, which is corrected for inclination effects. Right: same as the left panel, but with an observed luminosity function assumed to have indexes $\alpha = -0.8$ and $\beta = -4.5$. The comparison between the two panels shows that a greater difference between α and β accentuates the knee distortion and the variance between $m(\mathcal{L})$ and $n(L)$ at higher luminosities. For a better comparison, the red solid line of the left panel is also plotted in the right panel, in grey.

observed luminosity is $L = \mathcal{L}\cos\theta$, where $L = \mathcal{L}$ for face-on quasars and $L \to 0$ for those seen at increasingly large inclinations. Assuming the true quasar luminosity distribution in the Universe is a continuous function $m(\mathcal{L})$, and given that quasars are randomly inclined, a specific observed luminosity bin would contain objects with particular combinations of intrinsic luminosity and inclination angle. Hence, the observed distribution $n(L)$ can be expressed in terms of the intrinsic distribution $m(\mathcal{L})$:

$$n(L)\mathrm{d}L = \int_0^{\pi/2} m\left(\frac{L}{\cos\theta}\right)\sin\theta\,\mathrm{d}\theta\mathrm{d}\mathcal{L}. \tag{2}$$

Detailed calculations in Appendix A allow us to derive the true luminosity function $m(\mathcal{L})$ from the observed one, $n(L)$:

$$m(\mathcal{L}) = n(L) - n'(L)L. \tag{3}$$

The result of this correction is therefore the distribution of intrinsic quasar luminosities, which would be the observed distribution if all the objects were face-on. To properly compare with the observed $n(L)$, we multiply $m(\mathcal{L})$ by the average $\cos\theta$, which is 0.5. In Fig. 3, we show, as an example, the juxtaposition the observed $n(L)$ with the derived intrinsic luminosity function $m(\mathcal{L})$, assuming the quasar luminosity function shape from Ross et al. (2013),

$$\frac{\mathrm{d}n}{\mathrm{d}L} = \frac{\phi_*}{\left(\frac{L}{L^*}\right)^{-\alpha} + \left(\frac{L}{L^*}\right)^{-\beta}}, \tag{4}$$

with parameters α and β again following the results from Ross et al. (2013): $\alpha = -1.34$ and $\beta = -3.56$, and $\log(\phi_*) = -6.15$. As in the Ross et al. (2013) parametrisation, we assume the quasar luminosity function to follow a Pure Luminosity Evolution (PLE). In Fig. 3, as an example, we show the results assuming a redshift value of $z = 1$. Notably, at both low and high luminosities, the shape of the intrinsic luminosity function aligns with the observed one. The main differences are found around the change in the slope, commonly called the "knee". Altering the α and β values impacts the relative shapes: a greater difference between α and β accentuates the knee distortion and the variance between $m(\mathcal{L})$ and $n(L)$ at higher luminosities. The right panel of Fig. 3 showcases the results for $\alpha = -0.8$ and $\beta = -4.5$.

4.2. Mock sample

Now that we know how to derive an inclination-corrected luminosity function, we can use it to build our mock sample of quasars to determine the effect of inclination on the L_X–L_{UV} observed dispersion. We do so, at first, allowing the inclination angle to vary between 0 and $\pi/2$. This assumption is not truly realistic, as we know that objects with an inclination angle above a certain threshold are not going to be observed due to the presence of an obscuring torus (or, when they are, the selection procedure removes them from the sample). However, we perform this analysis to obtain an unbiased indication on the required torus opening angle.

We start building a sample of 100 000 objects, and we consider the quasar luminosity function obtained by Ross et al. (2013) for the SDSS as the starting point. Such a luminosity function assumes a redshift dependence. Therefore, we first assign a random redshift to the objects in the mock sample, extracting them from the redshift distribution of L20. Then, for each object, we derive the luminosity function corresponding to that redshift from Ross et al. (2013), we correct it for the inclination effect described in the previous subsection and we use it to extract a luminosity value for that object. The luminosity function described in Ross et al. (2013) is derived for the i-magnitude, but we are interested in the monochromatic luminosity at 2500 Å. Therefore, for each object, we derive it by assuming an SED with $f_\nu \sim \nu^{-\alpha}$, with $\alpha = 0.5$. We tested all of the following also assuming $\alpha = 1$ and we always obtained consistent results. Given the 2500 Å luminosities, we assume the L_X–L_{UV} relation with $\gamma = 0.6$ and derive the corresponding $\log(L_X)$ for each object. The values of $\log(L_X)$ are then shifted

by a random quantity extracted from a Gaussian with mean zero and standard deviation equal to 0.08; this mimics the contribution to the dispersion due to the variability, which, as we found out in Sect. 3, is $\delta_{\rm var} = 0.08$. Then, for each object, we assign a random value of the inclination angle θ, from 0 to $\pi/2$, as we are here assuming no absorbing torus. The angle is extracted from a distribution which is uniform in $\cos\theta$. Given θ, the inclined UV luminosity is derived as $L_{\rm obs} = \mathcal{L}\cos\theta$, while the X-ray luminosity is left untouched. We now have a mock sample of inclined objects and we have to consider the presence of an observational threshold. We consider as a threshold the *i*-magnitude flux limit of the first SDSS release (Richards et al. 2002), $m_i = 19.1$, from which we derived the corresponding monochromatic flux at 2500 Å[2]. So for each object, given its redshift, we derived its 2500 Å flux by assuming a standard flat ΛCDM cosmology and then removed the object from the mock sample if it fell below the threshold. We now fit the relation between $\log(L_{\rm X})$ and $\log(L_{\rm UV})$, where $L_{\rm UV}$ has the inclination-affected values. The fit is done with a Bayesian approach of likelihood maximisation, assuming the function $\log(L_{\rm X}) = \gamma \log L_{\rm UV} + \beta$, where γ and β are two free parameters, and where we take the presence of a dispersion δ into account by modifying the likelihood function accordingly. As before, we performed the fit using the *emcee* code. The mock sample and the results of the fit are shown in the top left panel of Fig. 4. We retrieve a slope coefficient $\gamma_{\rm fit} = 0.58 \pm 0.02$, consistent with the assumed value of $\gamma = 0.6$. This reassures us that the inclination effect is not significantly affecting the slope of the relation. The total dispersion is $\delta_{\rm tot} = 0.13$ dex. Given that we assumed a dispersion of $\delta_{\rm var} = 0.08$ dex due to the variability, to obtain the contribution of the inclination we have to quadratically subtract the two, so that $\delta_{\rm inc} = \sqrt{\delta_{\rm tot}^2 - \delta_{\rm var}^2}$. The result is $\delta_{\rm inc} = 0.10$ dex. On the top right panel of Fig. 4 we show, in green, the histogram of the fit residuals (which we obtain by simply subtracting the best-fit model from the mock data). In dot-dashed orange, we show the same histogram for the L20 sample. It is clear that the point distribution of our mock sample is not representative of the observed scenario, as it is (slightly) off-centred and significantly skewed, with a skewness parameter of $s = 1.18$, while the L20 distribution is much more symmetric, with a skewness parameter of $s_{\rm L20} = 0.20$. In the top right panel, we also show the distribution of the residuals for the silver and the golden samples of Sacchi et al. (2022), which is further discussed in Sect. 6.

To enhance the accuracy of our mock sample, we now introduce in our model an obscurer characterized by a maximum angle $\psi_{\rm torus}$, measured from the accretion disc as shown in the scheme in Fig. 2. We assume this torus to be a homogeneous dust distribution that extends from the plane of the accretion disc to $\psi_{\rm torus}$. Therefore, if a quasar has an inclination angle that exceeds $\theta_{\rm max} = \pi/2 - \psi_{\rm torus}$, the torus absorbs its emission, making it undetectable[3]. This results in an accessible angle range of $[0, \theta_{\rm max})$, instead of the initial $[0, \pi/2)$ range. We find that by increasing $\psi_{\rm torus}$, the histogram of the residuals becomes more and more symmetric. After some tests, we deduced that a $\theta_{\rm max}$ of ∼65° (which corresponds to an obscurer angle of $\psi_{\rm torus} = 25°$) is the maximum value that achieves a distribution of the residuals similar to the L20 sample, as visualized in the lower right panel of Fig. 4. This new histogram has a skewness parameter of $s = 0.19$, consistent with what we find for the L20 sample, which has $s_{\rm L20} = 0.20$. We note that the histogram of the residuals for L20 is wider because that sample has an overall dispersion of $\delta = 0.21$ dex, while our mock sample has $\delta = 0.10$ dex. The lower left panel of Fig. 4 displays the new fit. Due to the narrower angle range, objects disperse less around the best fit, resulting in a total dispersion of $\delta_{\rm tot} = 0.10$ dex. By considering this dispersion and subtracting the variability contribution quadratically, we obtain $\delta_{\rm inc} = 0.06$ dex. Given the match in the shape of the distribution of the residuals with the actual observed sample, we believe this to be a more reliable estimate of the inclination-related dispersion.

The concept of a toroidal absorber to describe the emission of quasars is not novel and it is a fundamental part of the AGN unified model (see for example Bianchi et al. 2012 for a review). At the same time, it is noteworthy that our mock sample necessitated an obscuring torus based solely on the comparison with the histogram of the residuals from the L20 sample, as this comes out as a somewhat indirect way to assess the minimum required angular width of the torus for an average population of quasars. In summary, our mock quasar sample analysis allows us to estimate the inclination contribution to the observed dispersion, approximating it at $\delta_{\rm inc} = 0.06$ dex.

We note that, in order to retrieve the intrinsic luminosity distribution, we could not start from the luminosity distribution of L20, as the latter is not only affected by inclination but also by additional filtering criteria that make the selection function very complex. As the latter effects cannot be corrected, we adopted instead the luminosity function of Ross et al. (2013) to build our mock sample. At the same time, it is important to note that the selection of L20 does not depend on the UV luminosity itself, so it should not alter the contribution of inclination to the total observed dispersion. To verify this assumption, we performed two additional tests. First, we estimated the dispersion contribution in small redshift bins ($\Delta z \sim 0.2$), in the redshift range of the L20 sample (which goes from $z \sim 0$ to $z \sim 5$). At all redshifts, the resulting contribution of the inclination to the final dispersion is $\delta_{\rm inc} \sim 0.06$ dex, confirming the absence of a luminosity trend in this contribution. As an additional test, we build another mock sample starting from the L20 luminosity distribution, and correcting that distribution for the inclination factor. We also assumed the L20 redshift distribution to derive the redshift, and performed all the steps described above. The results are shown in the appendix, and again a contribution of the inclination to the total dispersion of $\delta_{\rm inc} \sim 0.06$ dex is confirmed.

The results presented here demonstrate that the dispersion due to the inclination does not depend on luminosity or redshift and that, overall, we can safely consider its contribution to be $\delta_{\rm inc} \sim 0.06$ dex. Differences in the exact shape of the starting luminosity distribution for the mock sample do not seem to affect the estimate.

We finally note that, in this analysis, we assumed the same torus opening angle for all the objects in the sample. In principle, there might be a redshift dependence of the obscuration level of quasars, which would imply a different contribution of inclination at different redshifts. This evolution of the torus properties has been theorized to explain the observed trend of the

[2] The selection function for any observed sample is going to be much more complicated than a simple flux threshold. However, here we want to recreate a simpler scenario of a uniform sample with a given flux limit. We tested that the final results in terms of the inclination contribution to the dispersion do not depend on the exact choice of the flux limit.

[3] We basically assumed an infinite optical depth for the torus. This is not truly representative of the real scenario, but does not affect the consistency between our mock sample and the observed sample, as in the observed sample even mildly obscured objects are removed.

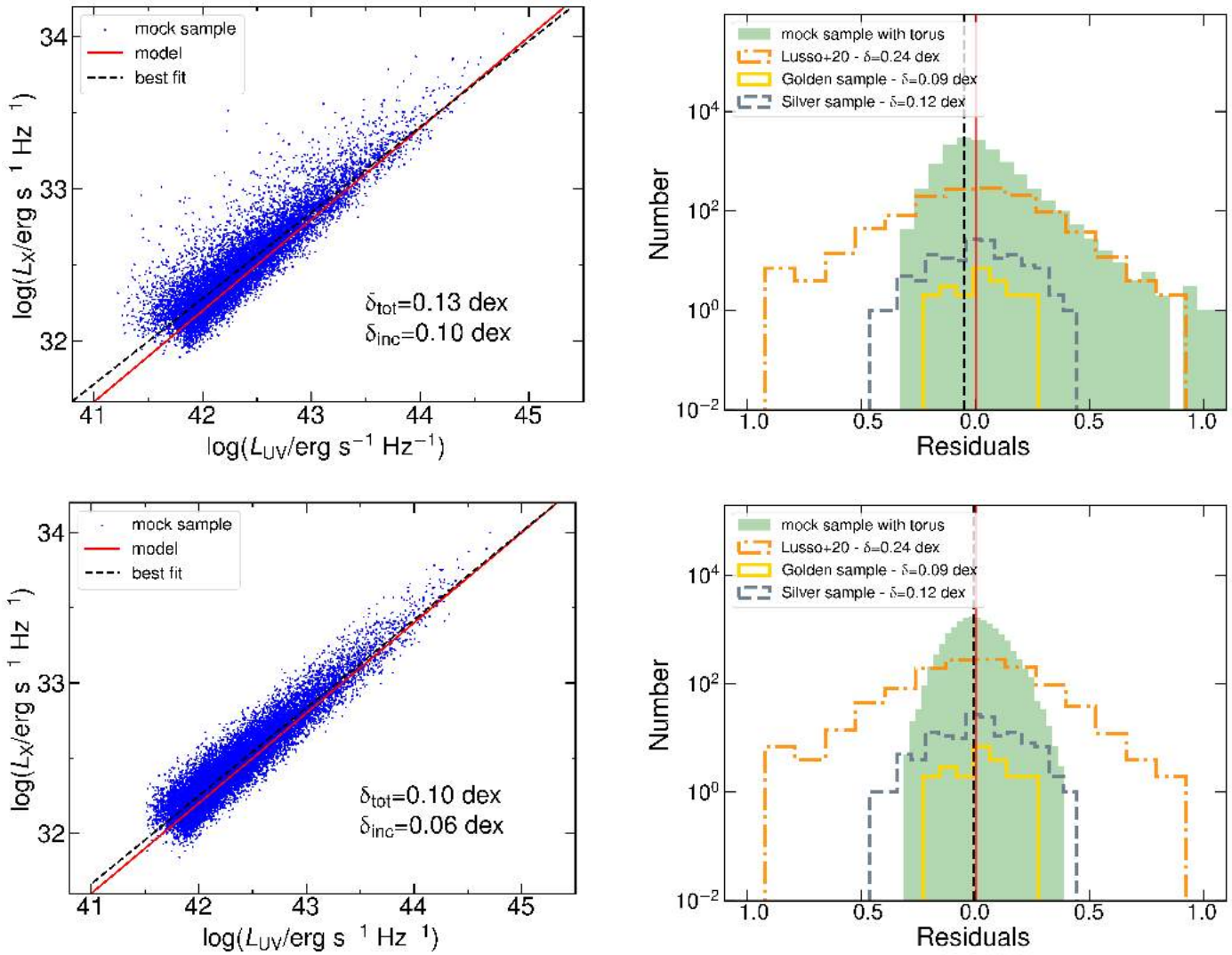

Fig. 4. L_X−L_{UV} relation and its spread for the two mock samples we considered, with and without the assumption of an obscuring torus. The residuals of the relation are also shown, in comparison with the results of the L20 and the Sacchi et al. (2022) samples. Upper left panel: mock sample of 100 000 quasars assuming an intrinsic relation with zero intrinsic dispersion, a contribution from variability to the observed dispersion of 0.08 dex, and an inclination angle between 0 and 90°. For each object, a redshift is assigned using the L20 sample redshift distribution; given the redshift, the corresponding luminosity function from Ross et al. (2013) is derived, and a luminosity is extracted. The red solid line is the starting sample, with a slope $\gamma = 0.6$ and a zero dispersion. The blue points show the sample after the dispersion due to variability is added and the objects are assigned a random inclination. The total dispersion of the sample is $\delta_{tot} = 0.13$ dex, the inclination effect accounts for $\delta_{inc} = 0.10$ dex. Upper right panel: histogram of the fit residuals, in filled green. This distribution is skewed, with a skewness parameter of $s = 1.18$. In dot-dashed orange, the histogram of the residuals for the L20 sample is shown for comparison. We see that the L20 distribution, which is the observed one, is instead much more symmetric, with a skewness parameter of $s_{L20} = 0.20$. The residuals corresponding to the "silver sample" and the "golden sample" of Sacchi et al. (2022) (details in Sect. 6) are plotted in dashed silver and in solid gold, respectively. The red solid vertical line corresponds to zero, while the dashed black vertical line corresponds to the peak of the mock sample distribution, equal to −0.05. All the histograms are shown in logarithmic units to enhance the readability. Lower left panel: same as the upper left panel, but assuming the presence of an obscurer with an angle width of $\psi_{torus} = 25°$, which means that the inclination angle for the objects in the mock sample can go from 0 to 65°. The total dispersion is reduced to $\delta_{tot} = 0.10$ dex, and the inclination effect accounts for $\delta_{inc} = 0.06$ dex. Lower right panel: same as the upper right panel, but assuming the presence of an obscurer with an angle width of $\psi_{torus} = 25°$. Here we see that the residuals distribution is symmetric, with a skewness parameter of $s = 0.19$ consistent with the L20 results.

obscured fraction of AGN, whereby high-redshift objects are more likely to be obscured than local ones (e.g. Liu et al. 2017; Iwasawa et al. 2020; Peca et al. 2023; Signorini et al. 2023b). However, recent results reveal no significant trend of the opening angle with cosmic time (e.g. Prince et al. 2022; Rałowski et al. 2024), and point towards a model where the increasing obscuration fraction is attributable to the evolution of the host-galaxy ISM properties (e.g. Gilli et al. 2022). Therefore, for the purpose of this work, the assumption of no redshift evolution of the inclination is reasonable, but further studies on this topic are necessary.

5. X-ray analysis

Finally, another potential source of observational dispersion might arise from the use of photometric data to calculate the 2-keV monochromatic luminosities of our objects, instead of spectroscopic data. In this section we show that this is not the case,

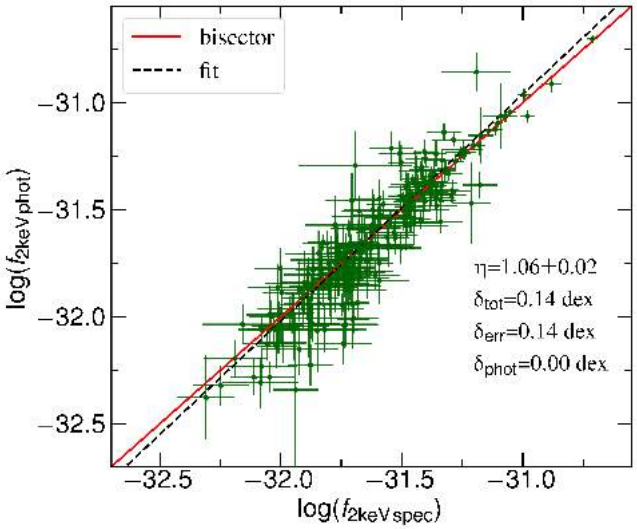

Fig. 5. Comparison of the 2-keV monochromatic flux estimate derived from photometric data (see L20) and the one derived from spectroscopic data for the subsample of objects with only one observation in the 4XMM-DR9 catalogue. The solid red line represents the bisector, while the black dashed line is the best fit, with a slope of $\eta = 1.06 \pm 0.02$. The total scatter around the best fit is equal to the average uncertainties, $\delta_{\rm err} = \delta_{\rm tot} = 0.14$ dex. The intrinsic dispersion of the relation is therefore zero. Overall, we can say that there is no significant contribution to the observed dispersion that comes from using photometric X-ray data instead of spectroscopic data.

and we can safely use photometric X-ray data. In Signorini et al. (2023a), we tested whether there is any offset between the photometric and spectroscopic flux determination. To do that, we performed the X-ray spectral analysis on a sample of 231 objects, which are all the quasars in the L20 catalogue with *XMM-Newton* observations and a redshift higher than 1.9. The findings indicate that employing photometrically derived fluxes (or luminosities) instead of spectroscopically derived ones does not introduce any significant offset. However, it is possible that photometrically derived fluxes exhibit a greater scatter around the true value compared to spectroscopically derived ones. If this were the case, our prevalent use of photometric data would not introduce any bias in determining the relation parameters, but it would still increase the observed dispersion.

To investigate this further, we used the X-ray spectroscopically analysed sample from Signorini et al. (2023a), and we tested the equation:

$$\log(f_{2\,\rm keV,\,spec}) = \eta \log(f_{2\,\rm keV,\,phot}) + \epsilon. \quad (5)$$

We employed the same fitting procedure described in Sect. 3. From the 231 sources, we removed the 38 that have multiple observations. Indeed, these objects have a photometric flux estimate that has been obtained by averaging multiple observations (Lusso & Risaliti 2016; L20), while the spectroscopic analysis has been performed on the longest observation only.

From the regression analysis, we obtained a slope close to unity ($\eta = 1.06 \pm 0.02$), as previously discussed in Signorini et al. (2023a). The fact that this value is different from one could imply a different final slope of the $L_{\rm X}$–$L_{\rm UV}$ relation. However, we checked that this is not the case, with results shown in Appendix C.

The results are illustrated in Fig. 5. We found both $\delta_{\rm tot}$ and $\delta_{\rm err}$ to be equal to 0.14 dex, indicating that the intrinsic dispersion $\delta_{\rm phot}$ is consistent with zero. The outcome of this analysis is clear: when comparing the spectroscopic and photometric 2 keV flux estimates for a subsample of objects where the same observations were used to derive both estimates, there is no additional dispersion beyond that arising from observational uncertainties. Consequently, utilising photometric data instead of spectroscopic ones does not introduce any offset or bias, nor does it contribute to the total observed dispersion. This finding supports the validity and reliability of employing photometrically derived fluxes (or luminosities) in our astrophysical analyses, which is particularly relevant considering that deriving spectroscopic X-ray monochromatic flux estimates for thousands of objects is very time-consuming.

Another potential issue with X-ray observations is their off-axis nature. The majority of X-ray data for the L20 sample is derived from serendipitous observations, exhibiting a mean off-axis angle for the *XMM-Newton* sources – which constitute most of the sample – of $\phi_{\rm off} \sim 6.4'$. The different distance of the targets from the detector aimpoint might introduce additional dispersion. This was tested on a subset of 1778 objects, corresponding to those with serendipitous *XMM-Newton* observations in the L20 sample. We examined the $L_{\rm X}$–$L_{\rm UV}$ relation across six off-axis angle bins: 0–2′, 2′–4′, 4′–6′, 6′–8′, 8′–10′, and 10′–12′. In each bin, we observed a dispersion of $\delta \sim 0.24$ dex, with no significant trend with respect to the off-axis angle. This suggests that the off-axis angle does not substantially contribute to the dispersion. However, it is important to note that when the observed dispersion is large, minor effects become hard to discern. Assuming that objects at an off-axis angle of ∼10′ have an additional dispersion factor of $\delta_{\rm off} \sim 0.04$ dex, this difference would be lost in a comparison with a sample having a smaller off-axis angle, since $\sqrt{0.24^2 - 0.04^2} \sim 0.24$.

One approach to further investigate this might involve analysing a subsample with a range of off-axis values but a lower observed dispersion, such as the golden sample from Sacchi et al. (2022). However, in the golden sample, objects with a smaller off-axis angle (the pointed objects from Nardini et al. 2019) also exhibit significantly higher average luminosity compared to those at a greater off-axis angle. Given this, along with the small overall statistics for this sample, we cannot confidently distinguish the effect of lower variability due to higher average luminosity from the potential reduction of the dispersion due to pointed observations. Future targeted observations on selected subsamples might provide clearer insights into the actual impact of off-axis observations (Lusso 2019). We also note that on-axis objects show a significantly lower uncertainty on flux measurements (∼2%) compared to off-axis objects with similar luminosities (∼5%). Lower uncertainties mean a lower total dispersion, which makes it possible to characterise smaller contributions to the observed dispersion. Therefore, pointed observations are always ideal. For now, we can conclude that if this effect exists, it is likely a minimal contribution, with $\delta_{\rm off} \leq 0.04$ dex.

6. Comparison with observational results

We have determined that the contribution from X-ray variability to the dispersion is approximately $\delta_{\rm var} \sim 0.08$ dex. It is also evident that low-luminosity objects exhibit a greater contribution than their high-luminosity counterparts. Furthermore, our findings indicate that the use of X-ray photometric data does not introduce any additional dispersion to the relation. Through the construction of mock samples, we have determined that the inclination of the quasar's accretion disc relative to our line of sight contributes to the total observed dispersion with $\delta_{\rm inc} \sim 0.06$ dex. Therefore, the sources of dispersion we have assessed collectively contribute with a residual dispersion of

$\delta_{\rm res} = \sqrt{0.06^2 + 0.08^2} = 0.10$ dex. We can now compare these results with the most recent estimates of the observed dispersion.

Firstly, we consider the results of Signorini et al. (2023a). In that study, using UV spectroscopic data and the best UV and X-ray proxies for the correlation, which were found to be the MgII line flux and the monochromatic 1 keV flux, respectively, a dispersion of $\delta_{\rm obs} = 0.16$ dex was found. When compared to our current estimate of the residual dispersion $\delta_{\rm res} = 0.10$ dex, it is evident that the characteristic dispersion of the correlation must be less than $\delta_{\rm char} \leq \sqrt{\delta^2_{\rm obs} - \delta^2_{\rm res}} = 0.12$ dex.

The work of Sacchi et al. (2022) offers additional clues. They presented a sample of 130 quasars, a subsample of the L20 one, with high-quality data and a one-by-one UV and X-ray spectral analysis. This sample, which we call here the "silver sample", showed a dispersion of $\delta_{\rm silver} = 0.12$ dex. Within this sample, they also highlighted a subsample of 30 objects at redshift $z \sim 3$, referred to as the "golden sample", with an even lower observed dispersion, $\delta_{\rm golden} = 0.09$ dex. We display the residuals with respect to the $L_{\rm X}$–$L_{\rm UV}$ relation for these two samples in the right panels of Fig. 4, alongside the residuals for the mock samples and for the whole L20 sample discussed previously. Considering the silver sample, up to 0.10 dex of its dispersion can be attributed to variability and inclination. Hence, the intrinsic dispersion for the relation is estimated to be $\delta_{\rm char} \leq \sqrt{0.12^2 - 0.10^2} \sim 0.07$ dex. For the golden sample, its dispersion is already smaller than the total of 0.10 dex which we found to be attributable to variability and inclination. This can be explained in terms of the sample high average luminosity, $\log(L_{\rm X}/{\rm erg\,s^{-1}\,Hz^{-1}}) \sim 27.7$. Consequently, the overall variability contribution to the dispersion is minimal, approximately $\delta_{\rm var,H.L.} \sim 0.02$ dex, as detailed in Sect. 3. The intrinsic dispersion of the $L_{\rm X}$–$L_{\rm UV}$ relation for the golden sample can therefore be estimated as $\delta_{\rm char} \leq \sqrt{0.09^2 - 0.06^2 - 0.02^2} \sim 0.06$ dex. Remarkably, the estimates for both subsamples are similar.

To sum up, when examining the entire quasar sample, data-quality constraints limit us to a dispersion no lower than 0.21 dex for the L20 data set and 0.16 dex for the Signorini et al. (2023a) one (utilising UV spectroscopic data along with the optimal proxies for UV and X-ray emission). Of this total dispersion, 0.10 dex is attributable to the combined impact of variability and inclination. In cases of high-quality data, the dispersion can drop to 0.12 dex when the variability contribution is still significant, and to 0.09 dex when high luminosities reduce the variability contribution, as demonstrated in Sacchi et al. (2022). From these analyses, we deduce that the characteristic dispersion of the $L_{\rm X}$–$L_{\rm UV}$ relation must be equal to or lower than $\delta_{\rm int} \sim 0.06$.

7. Comment on the possible theoretical models

As previously mentioned, we still lack a universally accepted physical model to explain the $L_{\rm X}$–$L_{\rm UV}$ relation, and why it is so tight. However, several models have been suggested in the past years. For instance, Lusso & Risaliti (2017) proposed a "toy model" for the relation based on a geometrically thin, optically thick accretion disc with a uniform, magnetized X-ray corona, as suggested by Svensson & Zdziarski (1994) and Merloni & Fabian (2002). By assuming that the corona is powered by the disc at a certain transition radius (where the gas pressure equals the radiation pressure), the authors find that both the UV and X-ray luminosities depend on the black hole mass $M_{\rm BH}$ and accretion rate $\dot{M}_{\rm BH}$. Assuming then the BLR radius–luminosity relation as $R_{\rm BLR} \propto L^{0.5}_{\rm bol}$, the black hole mass can be written as a function of the accretion rate and the broad-line FWHM, which finally leads to $L_{\rm X} \propto L^{4/7}_{\rm UV} \nu^{4/7}_{\rm FWHM}$. The expected slope value $\gamma = 4/7 \sim 0.57$ is very close to the observed one. At the same time, we would expect from this model a relation between the UV luminosity and the line FWHM, which was not confirmed by Signorini et al. (2023a) when considering the relation in fluxes.

Kubota & Done (2018) proposed a model for the optical–UV and X-ray emission based on an outer standard disc, an inner optically thick disc where warm Comptonisation produces the soft X-ray excess, and a hot optically thin corona. In this model, the X-ray luminosity is a fixed fraction of the bolometric luminosity, and the $L_{\rm X}$–$L_{\rm UV}$ relation emerges naturally as $\log(L_{\rm X}) = 3/4\log(L_{\rm UV}) - 2\log(\dot{m}) + b$, where the differences in the accretion rate $\dot{M}_{\rm BH}$ are what causes the observed dispersion of the relation. However, the theoretical slope of $\gamma = 0.75$ is not consistent with the observed values of $\gamma \sim 0.6$, and the model predicts a larger dispersion at higher luminosities, which we do not observe. In conclusion, there has not yet been a model whose predictions in terms of slope and dispersion of the relation match the observed values, and further studies are still needed to understand the exact coupling between the accretion disc and the corona.

8. Conclusions

In this paper, we have investigated the factors that might contribute to the residual dispersion of the $L_{\rm X}$–$L_{\rm UV}$ relation in quasars but cannot be removed by selecting unbiased samples. We identified three possible dispersion sources:

Variability: quasar emission is known to be variable both in the UV and in the X-ray bands, which inevitably causes an increase in the observed dispersion. Given the shorter timescales, X-ray variability is the one that is going to predominantly affect our results. To test the contribution of variability, we selected the 289 objects in the L20 sample that have multiple X-ray observations in the *XMM-Newton* 4XMM-DR9 catalogue. We found that the average scatter between different estimates of the 2-keV monochromatic luminosity, once measure uncertainties are accounted for, is $\delta_{\rm var} \sim 0.08$ dex, which we can therefore consider as the variability contribution. We also found, consistently with literature results, that variability decreases with increasing luminosity, with the high-luminosity subsample having a contribution of only $\delta_{\rm var,H.L.} = 0.02$ dex from variability to the total observed dispersion.

Inclination: the inclination of the accretion disc is believed to affect the observed UV luminosity, but not the X-ray one. Therefore, the different quasar inclinations introduce a scatter in the $L_{\rm X}$–$L_{\rm UV}$ relation. Unfortunately, we do not have observational methods to measure inclination and correct the UV luminosities accordingly. Therefore, we relied on mock-sample estimates to derive the inclination contribution to the observed dispersion. We discussed how to recover the intrinsic luminosity distribution given an observed one, correcting for the inclination effect. Starting from the Ross et al. (2013) luminosity function, we then built a mock sample of quasars for which we found the inclination contribution to the dispersion to be $\delta_{\rm inc} \sim 0.06$ dex, once we account for the presence of an obscuring torus at large inclinations.

X-ray photometry: in a previous work of this series (Signorini et al. 2023a), we have shown that using photometric estimates of the 2-keV monochromatic luminosities instead of spectroscopic ones does not introduce any systematic offset. However, it might still introduce an additional dispersion. In this work we tested this effect for a sample of 193 objects at redshift $z > 1.9$, and we found that photometric estimates do not introduce additional scatter compared to spectroscopic ones. Even though the observed scatter is larger with photometric measurements,

this is entirely accounted for by the larger uncertainties in the photometric data with respect to spectroscopic ones. This allows us to use photometric data when spectroscopic ones are not available, confident that we are not introducing additional dispersion.

Comparing our results with recent observational estimates of the dispersion from Sacchi et al. (2022), we conclude that the characteristic dispersion of the L_X−L_{UV} relation is exceedingly low, $\delta_{char} \leq 0.06$. This finding reinforces the hypothesis that the physical mechanism governing the L_X−L_{UV} relation is remarkably consistent across a broad range of redshifts and luminosities. This outcome gives additional credibility to using quasars as standard candles in cosmological studies, and it particularly highlights the significant tension existing with the flat ΛCDM cosmological model. The findings on variability confirm the results presented in Sacchi et al. (2022): subsamples with higher luminosities tend to exhibit the lowest observed dispersion values.

Although we can account for the dispersion of the L_X−L_{UV} relation down to ≤0.06 dex, the observed value for the adopted sample of quasars is still much higher. Obtaining such a small dispersion observationally would give significant additional cosmological power to quasars. On the one hand, we could try to reduce the variability contribution by obtaining multiple X-ray observations within weeks/months (which is roughly the variability timescale for the UV band), and average the X-ray fluxes. Unfortunately, given that the L20 sample (and any foreseeable cosmological sample) contains thousands of objects, this is not viable in the short run. Using simultaneous X-ray and UV observations has not proven to be helpful, because of the lag between the changes in one band and the consequential changes in the other (e.g. Vagnetti et al. 2011; Lusso & Risaliti 2016).

High-luminosity objects show a smaller variability amplitude than low-luminosity ones. Therefore, at the moment, the only way possible to reduce the variability contribution to the overall dispersion is to look at high-luminosity subsamples, as the golden sample presented in Sacchi et al. (2022). Regarding the inclination contribution to the dispersion, we have no way to remove it until a reliable means to estimate the inclination angle for each individual object is found. It might be argued that the brightest objects at any redshift are predominantly seen (nearly) face-on, since a high inclination angle would imply an intrinsic luminosity far exceeding the Eddington limit. Yet, there is no definitive method to determine the specific luminosity threshold at which an object can be classified as face-on. In terms of X-ray observations, a possible reduction of the dispersion might come from having more pointed observations instead of serendipitous ones, but further analysis is needed with this respect.

Overall, the best path in the short-term to obtain small dispersion values in the L_X−L_{UV} relation and to increase the cosmological power of quasars is to obtain pointed observations of the most luminous quasars at the highest possible redshift. This can enhance our understanding of the high-redshift Hubble diagram and of the associated cosmological tensions.

In the more distant future, the combination of the X-ray data from Athena (or other proposed X-ray facilities) with the optical/UV data that are starting to be collected by *Euclid* (Laureijs et al. 2011) and LSST (Ivezić et al. 2019), will provide additional statistics, helping us characterise the L_X−L_{UV} relation both physically and for its cosmological implementation.

Acknowledgements. The authors would like to thank the referee for their comments and suggestions, which significantly improved the paper.

References

Akritas, M. G., & Bershady, M. A. 1996, ApJ, 470, 706
Bañados, E., Venemans, B. P., Mazzucchelli, C., et al. 2018, Nature, 553, 473
Bargiacchi, G., Risaliti, G., Benetti, M., et al. 2021, A&A, 649, A65
Bargiacchi, G., Benetti, M., Capozziello, S., et al. 2022, MNRAS, 515, 1795
Bianchi, S., Maiolino, R., & Risaliti, G. 2012, Adv. Astron., 2012, 782030
Bisogni, S., Marconi, A., & Risaliti, G. 2017, MNRAS, 464, 385
Boyle, B. J., Shanks, T., Croom, S. M., et al. 2000, MNRAS, 317, 1014
Croom, S. M., Richards, G. T., Shanks, T., et al. 2009, MNRAS, 399, 1755
de Vries, W. H., Becker, R. H., White, R. L., & Loomis, C. 2005, AJ, 129, 615
Elvis, M., Hao, H., Civano, F., et al. 2012, ApJ, 759, 6
Foreman-Mackey, D., Hogg, D. W., Lang, D., & Goodman, J. 2013, PASP, 125, 306
Giambagli, L., Fanelli, D., Risaliti, G., & Signorini, M. 2023, A&A, 678, A13
Gianolli, V. E., Kim, D. E., Bianchi, S., et al. 2023, MNRAS, 523, 4468
Gilli, R., Norman, C., Calura, F., et al. 2022, A&A, 666, A17
Gliozzi, M., & Williams, J. K. 2020, MNRAS, 491, 532
Hook, I. M., McMahon, R. G., Boyle, B. J., & Irwin, M. J. 1994, MNRAS, 268, 305
Ivezić, Ž., Kahn, S. M., Tyson, J. A., et al. 2019, ApJ, 873, 111
Iwasawa, K., Comastri, A., Vignali, C., et al. 2020, A&A, 639, A51
Kelly, B. C., Bechtold, J., & Siemiginowska, A. 2009, ApJ, 698, 895
Kubota, A., & Done, C. 2018, MNRAS, 480, 1247
Laureijs, R., Amiaux, J., Arduini, S., et al. 2011, ArXiv e-prints [arXiv:1110.3193]
Lanzuisi, G., Ponti, G., Salvato, M., et al. 2014, ApJ, 781, 105
Liu, T., Tozzi, P., Wang, J., et al. 2017, AJ, 232, 8
Lusso, E. 2019, Astron. Nachr., 340, 267
Lusso, E., & Risaliti, G. 2016, ApJ, 819, 154
Lusso, E., & Risaliti, G. 2017, A&A, 602, A79
Lusso, E., Comastri, A., Vignali, C., et al. 2010, A&A, 512, A34
Lusso, E., Risaliti, G., Nardini, E., et al. 2020, A&A, 642, A150
Markowitz, A., & Edelson, R. 2004, ApJ, 617, 939
Merloni, A., & Fabian, A. C. 2002, MNRAS, 332, 165
Mortlock, D. J., Warren, S. J., Venemans, B. P., et al. 2011, Nature, 474, 616
Nardini, E., Lusso, E., Risaliti, G., et al. 2019, A&A, 632, A109
Paolillo, M., Papadakis, I., Brandt, W. N., et al. 2017, MNRAS, 471, 4398
Peca, A., Cappelluti, N., Urry, C. M., et al. 2023, ApJ, 943, 162
Ponti, G., Papadakis, I., Bianchi, S., et al. 2012, A&A, 542, A83
Prince, R., Hryniewicz, K., Panda, S., Czerny, B., & Pollo, A. 2022, ApJ, 925, 215
Prokhorenko, S. A., Sazonov, S. Y., Gilfanov, M. R., et al. 2024, MNRAS, 528, 5972
Rałowski, M., Hryniewicz, K., Pollo, A., & Stawarz, Ł. 2024, A&A, 682, A120
Richards, G. T., Fan, X., Newberg, H. J., et al. 2002, AJ, 123, 2945
Richards, G. T., Lacy, M., Storrie-Lombardi, L. J., et al. 2006, ApJS, 166, 470
Risaliti, G., & Lusso, E. 2015, ApJ, 815, 33
Risaliti, G., & Lusso, E. 2019, Nat. Astron., 3, 272
Ross, N. P., McGreer, I. D., White, M., et al. 2013, ApJ, 773, 14
Sacchi, A., Risaliti, G., Signorini, M., et al. 2022, A&A, 663, L7
Sanders, D. B., Phinney, E. S., Neugebauer, G., Soifer, B. T., & Matthews, K. 1989, ApJ, 347, 29
Shakura, N. I., & Sunyaev, R. A. 1973, A&A, 24, 337
Signorini, M., Risaliti, G., Lusso, E., et al. 2023a, A&A, 676, A143
Signorini, M., Marchesi, S., Gilli, R., et al. 2023b, A&A, 676, A49
Sobolewska, M. A., & Done, C. 2007, MNRAS, 374, 150
Steffen, A. T., Strateva, I., Brandt, W. N., et al. 2006, AJ, 131, 2826
Svensson, R., & Zdziarski, A. A. 1994, ApJ, 436, 599
Tananbaum, H., Avni, Y., Branduardi, G., et al. 1979, ApJ, 234, L9
Uttley, P., McHardy, I. M., & Vaughan, S. 2005, MNRAS, 359, 345
Vagnetti, F., Turriziani, S., & Trevese, D. 2011, A&A, 536, A84
Vanden Berk, D., Wilhite, B., Kron, R., et al. 2004, Am. Astron. Soc. Meet. Abstr., 205, 120.02
Vaughan, S., Edelson, R., Warwick, R. S., & Uttley, P. 2003, MNRAS, 345, 1271
Wang, F., Yang, J., Fan, X., et al. 2021, ApJ, 907, L1
Webb, N. A., Coriat, M., Traulsen, I., et al. 2020, A&A, 641, A136
Young, M., Elvis, M., & Risaliti, G. 2009, ApJ, 183, 17
Young, M., Elvis, M., & Risaliti, G. 2010, ApJ, 708, 1388

Appendix A: Correction of the Luminosity Function for inclination effects

In this Appendix we report how we derive the intrinsic luminosity function $m(\mathcal{L})$ from the observed one, $n(L)$. We recall that the observed luminosity function consists of objects where the inclination effect has modified each object's observed luminosity, while we are interested in recovering the intrinsic luminosity distribution. We start from the relation between $n(L)$ and $m(\mathcal{L})$:

$$n(L)dL = \int_0^{\pi/2} m\left(\frac{L}{\cos\theta}\right)\sin\theta\, d\theta d\mathcal{L}. \tag{A.1}$$

We substitute $\cos\theta = x$ and $dx = -\sin\theta\, d\theta$:

$$n(L) = \int_0^1 m(L/x)dx. \tag{A.2}$$

We can now write that $L/x = \mathcal{L}$ and $-(L/x^2)\,\mathrm{d}x = \mathrm{d}\mathcal{L}$ so that

$$n(L) = \int_L^\infty m(\mathcal{L})\frac{L}{\mathcal{L}^2}d\mathcal{L}. \tag{A.3}$$

We derive with respect to L:

$$\frac{\partial}{\partial L}n(L) = \frac{\partial}{\partial L}\int_L^\infty m(\mathcal{L})\frac{L}{\mathcal{L}^2}d\mathcal{L} = \int_L^\infty \frac{m(\mathcal{L})}{\mathcal{L}^2}d\mathcal{L} - \frac{m(L)}{L}, \tag{A.4}$$

and then derive again:

$$\frac{\partial^2}{\partial L^2}n(L) = -\frac{m(L)}{L^2} - \frac{Lm'(L) - m(L)}{L^2} = -\frac{m'(L)}{L}, \tag{A.5}$$

from which:

$$m(\mathcal{L}) = \int_L^\infty n''(\mathcal{L})\mathcal{L}d\mathcal{L}, \tag{A.6}$$

and finally get:

$$m(\mathcal{L}) = n(L) - n'(L)L. \tag{A.7}$$

Appendix B: L20 luminosity distribution

We provide here the fit of the L_X–L_{UV} relation and the histograms of the residuals for the mock samples derived by starting from L20 luminosity distribution. In Fig. B.1 we show the results obtained without the torus assumption in the upper panel, and with the assumption of a torus with an angular width of $\psi_{torus} = 25°$ in the lower panels. The histograms scale is set to logarithmic to better visualise the different shapes. In the upper left panel we see that without the torus assumption, we obtain a large dispersion due to the inclination, $\delta_{inc} = 0.19$ dex, and a slope of the relation equal to $\gamma = 0.46 \pm 0.01$, not consistent with the value of $\gamma = 0.6$ assumed for the mock sample. In the upper right panel we also see that, as in the case discussed in the text where we started from the Ross et al. (2013) luminosity function, without the torus we obtain a highly skewed histogram of the residuals, with a skewness parameter of $s = 1.74$. The peak of the histogram is also shifted from zero, as it is found at -0.1.

In the lower panels, we show the results obtained assuming a $\psi_{torus} = 25°$ torus. In the lower left panel, we see that the best fit slope is now $\gamma = 0.60 \pm 0.01$, perfectly consistent with the assumed value of $\gamma = 0.6$. We note that, with this assumption, the dispersion due to inclination is estimated to be $\delta_{inc} = 0.06$ dex, which is the same value we obtain starting from Ross et al. (2013) luminosity distribution. In the lower right panel, we now see that the histogram of the residuals is symmetric, with a skewness parameter of $s = 0.20$ and a peak corresponding to -0.06.

To sum up, starting with the L20 luminosity distribution instead of the Ross et al. (2013) luminosity function, we obtain the same results in terms of both the need for a $\psi_{torus} \sim 25°$ torus, and the estimate of the contribution of inclination to the total dispersion, with $\delta_{inc} = 0.06$. This result shows us that our estimate for the inclination contribution does not strongly depend on the exact shape of the starting luminosity distribution.

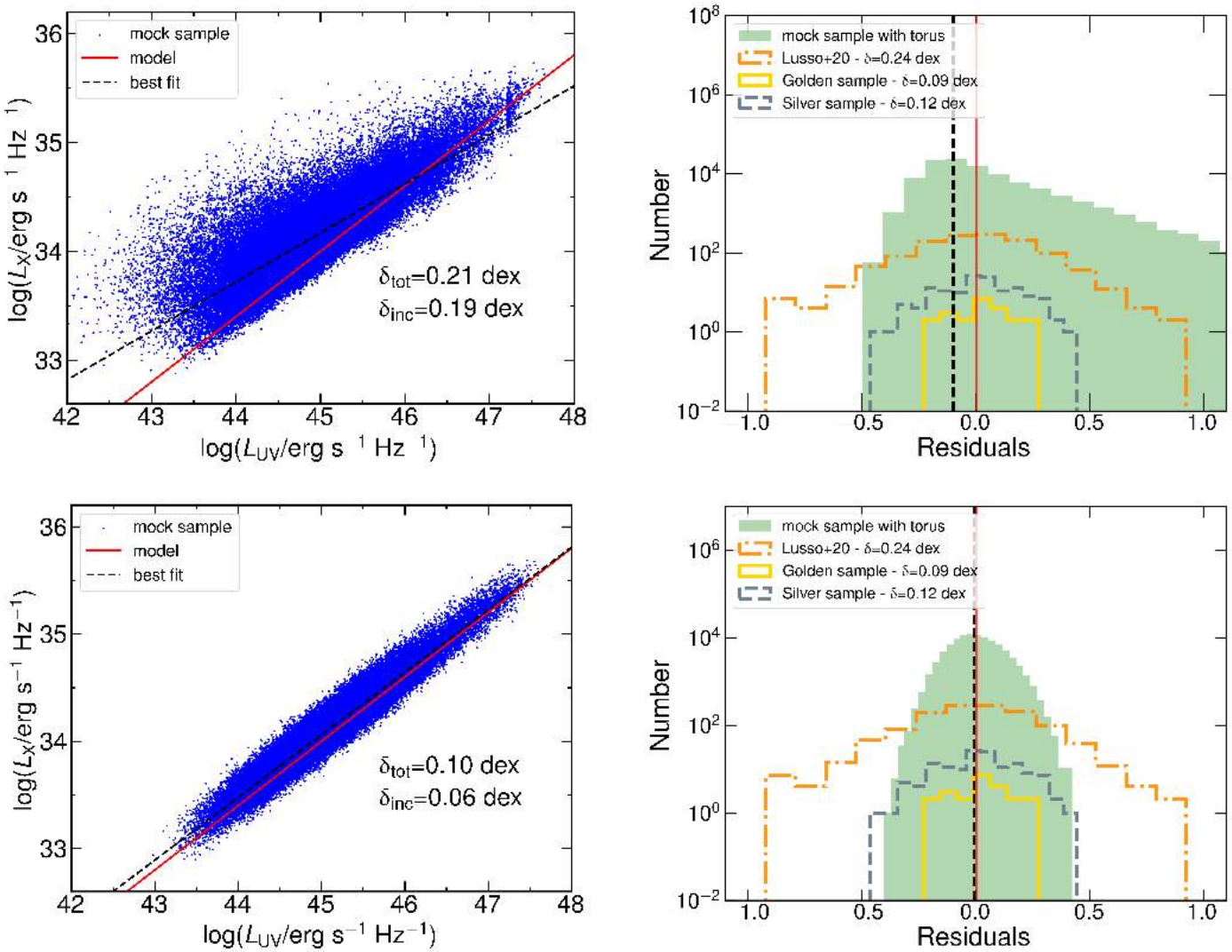

Fig. B.1. *Upper left panel*: mock sample of 100,000 quasars assuming a L_X−L_{UV} relation with zero intrinsic dispersion, a contribution from variability to the observed dispersion of 0.08 dex, and an inclination angle between 0 and $\pi/2$. For each object, a redshift is assigned using the redshift distribution of the L20 sample. To derive the luminosity, we correct the L20 luminosity distribution for the inclination effect. The red solid line represents the starting sample, with a slope $\gamma = 0.6$ and a zero dispersion. The blue points show the sample after the dispersion due to variability is added and the objects are assigned a random inclination. The total dispersion of the sample is $\delta_{tot} = 0.21$ dex, and the inclination effect accounts for $\delta_{inc} = 0.19$ dex. *Upper right panel*: histogram of the fit residuals, in filled green. This distribution has a skewness parameter of $s = 1.74$, and the peak is shifted from zero, at −0.16. In dot-dashed orange, the histogram of the residuals for the L20 sample is shown. We see that the L20 distribution, which is the observed one, is instead much more symmetric, with a skewness parameter of $s_{L20} = 0.20$. The histograms of the residuals for the silver sample and the golden sample of Sacchi et al. (2022) (details in Section 6) are also shown. The red solid vertical line corresponds to zero, while the dashed black vertical line corresponds to the peak of the mock sample distribution, equal to −0.16. *Lower left panel*: same as the upper Left panel, but assuming the presence of an obscurer with an angular width of $\psi_{torus} = 25°$, which means that the inclination angle for the objects in the mock sample can go from 0 to 65°. The total dispersion is reduced to $\delta_{tot} = 0.10$ dex, and the inclination effect accounts for $\delta_{inc} = 0.06$ dex. *Lower right panel*: same as the upper right panel, but assuming the presence of an obscurer with an angular width of $\psi_{torus} = 25°$. Here we see that the residuals distribution is symmetric, with a skewness parameter of $s = 0.20$, which perfectly matches the L20 value of $s_{L20} = 0.20$. We also note that the residuals distribution is now slightly wider than the one for the Sacchi et al. (2022) sample.

Appendix C: Additional material

When comparing, in Section 5, photometric and spectroscopic flux estimates, we obtain a slope of $\eta = 1.06 \pm 0.02$. In principle, this could imply a different slope of the $L_X - L_{UV}$ relation, when using the two different proxies. We tested the $L_X - L_{UV}$ relation, assuming a standard ΛCDM model to derive luminosities, with spectroscopic and photometric X-ray luminosities, to test if this was the case. The results are shown in Figure C.1. The slope that we obtain is $\alpha = 0.59 \pm 0.04$ for the spectroscopic luminosity and $\alpha = 0.58 \pm 0.03$ for the photometric one, so they are fully consistent.

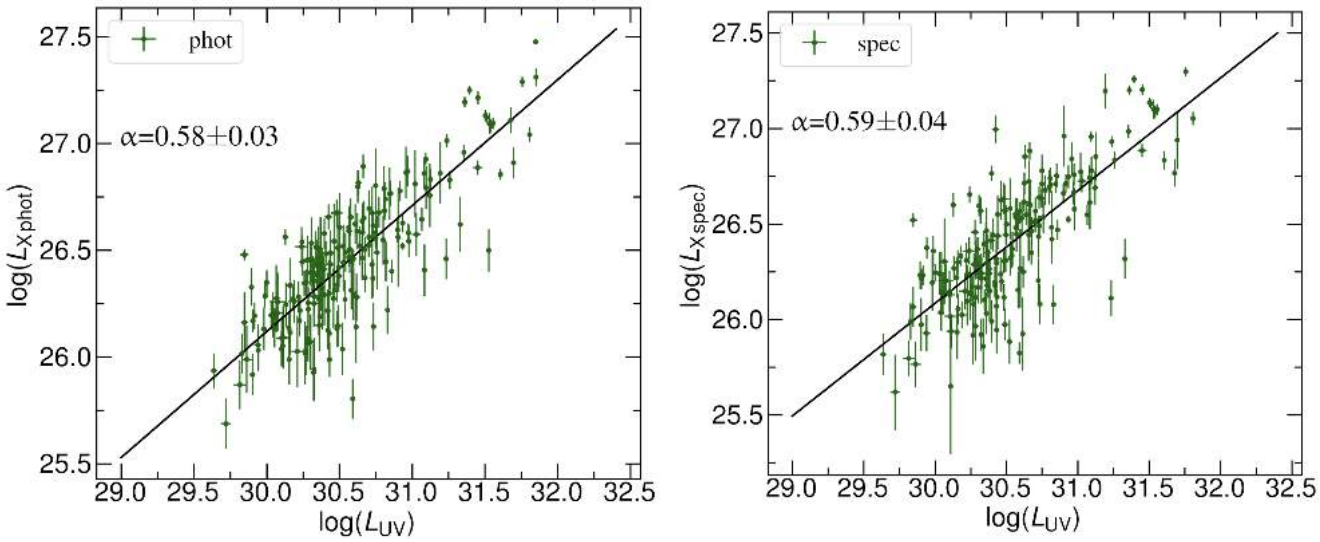

Fig. C.1. In this figure we compare the results of the $L_X - L_{UV}$ relation when using photometric or spectroscopic luminosity measurements for the X-ray luminosity. *Left panel*: fit of the $L_X - L_{UV}$ relation using the photometric X-ray luminosities, for the sample of 193 objects described in Section 5. A standard ΛCDM model is used to estimate luminosities from fluxes. We obtain a slope $\alpha = 0.58 \pm 0.03$. *Right panel*: same as the left panel, but using the spectroscopic estimate of the 2 keV luminosity. The obtained slope is $\alpha = 0.59 \pm 0.04$, fully consistent with the photometric one.